DWM07 global empirical model of upper thermospheric storm-induced disturbance winds

J. T. Emmert,[1] D. P. Drob,[1] G. G. Shepherd,[2] G. Hernandez,[3] M. J. Jarvis,[4] J. W. Meriwether,[5] R. J. Niciejewski,[6] D. P. Sipler,[7] and C. A. Tepley[8]

[1]   We present a global empirical disturbance wind model (DWM07) that represents average geospace-storm-induced perturbations of upper thermospheric (200–600 km altitude) neutral winds. DWM07 depends on the following three parameters: magnetic latitude, magnetic local time, and the 3-h Kp geomagnetic activity index. The latitude and local time dependences are represented by vector spherical harmonic functions (up to degree 10 in latitude and order 3 in local time), and the Kp dependence is represented by quadratic B-splines. DWM07 is the storm time thermospheric component of the new Horizontal Wind Model (HWM07), which is described in a companion paper. DWM07 is based on data from the Wind Imaging Interferometer on board the Upper Atmosphere Research Satellite, the Wind and Temperature Spectrometer on board Dynamics Explorer 2, and seven ground-based Fabry-Perot interferometers. The perturbation winds derived from the three data sets are in good mutual agreement under most conditions, and the model captures most of the climatological variations evident in the data.

1.   Introduction

[2]   The thermospheric neutral wind is a key component of the ionosphere-thermosphere (I-T) system. Winds fundamentally influence the composition and dynamics of both the neutral and ionized components of the upper atmosphere, as well as electric fields and currents. However, wind measurements in the thermosphere are too sparse to permit specification of the global wind field at a given time from synoptic measurements. Empirical characterizations of wind patterns based on past statistical behavior are therefore important resources: They provide dynamical information when measurements are not available, facilitate interpretation of the behavior of other I-T components, and serve as a benchmark for validation of new wind measurements and of numerical models.

[3]   Accurate predictions of thermospheric winds are particularly difficult to obtain under geomagnetically disturbed conditions. During geospace storms and substorms, the I-T system is perturbed by enhanced magnetospheric energy input (see *Rees* [1995] and *Fuller-Rowell et al.* [1997] for descriptions of the physical processes that produce the neutral dynamical response). Numerous case studies of storm time neutral dynamics have been conducted using data from a wide variety of instruments and modeling simulations [e.g., *Hernandez and Roble*, 1976; *Forbes et al.*, 1987; *Burns et al.*, 1995; *Emery et al.*, 1999; *Sutton et al.*, 2005]. Models have also been used to simulate the response of thermospheric winds to idealized storms [e.g., *Richmond and Matsushita*, 1975; *Fuller-Rowell et al.*, 2002; *Deng and Ridley*, 2006, and references therein]. Although coupled I-T general circulation models reproduce the major features of the observed neutral wind response [e.g., *Crowley et al.*, 1989; *Emery et al.*, 1999], a systematic validation of their predictions has yet to be conducted.

[4]   *Hedin et al.* [1988] developed the first global empirical thermospheric wind model, Horizontal Wind Model 87 (HWM87), using upper thermospheric wind measurements by Atmospheric Explorer E (AE-E) and Dynamics Explorer 2 (DE 2). HWM87 includes a rudimentary dependence on geomagnetic activity level, similar to that of the MSIS-86 empirical model of thermospheric density and temperature [*Hedin*, 1987]. The geomagnetic activity terms only provide a low-resolution modulation of the HWM87 quiet time patterns (incomplete data coverage under disturbed conditions precluded a more detailed representation). For the next version of the model, HWM90, *Hedin et al.*

[1]Space Science Division, U.S. Naval Research Laboratory, Washington, D.C., USA.
[2]Centre for Research in Earth and Space Science, York University, North York, Ontario, Canada.
[3]Department of Earth and Space Sciences, University of Washington, Seattle, Washington, USA.
[4]British Antarctic Survey, Cambridge, UK.
[5]Department of Physics and Astronomy, Clemson University, Clemson, South Carolina, USA.
[6]Space Physics Research Laboratory, University of Michigan, Ann Arbor, Michigan, USA.
[7]Haystack Observatory, Massachusetts Institute of Technology, Westford, Massachusetts, USA.
[8]Arecibo Observatory, Cornell University, Arecibo, Puerto Rico.

[1991] incorporated ground-based thermospheric wind measurements and increased the spatial resolution of the geomagnetic activity dependence. The most recent version, HWM93 [*Hedin et al.*, 1996], extends the model to the ground, but its thermospheric winds are the same as HWM90.

[5] Since the development of the early HWM models, new and extensive upper thermospheric wind databases have been generated by the Wind Imaging Interferometer (WINDII) [*Shepherd et al.*, 1993] on board the Upper Atmosphere Research Satellite (UARS) and by various ground-based instruments. It has therefore been possible to improve the statistical characterization of geospace storm effects on upper thermospheric winds. Several regional statistical studies of storm effects have been conducted [*Sica et al.*, 1986; *Hernandez et al.*, 1991; *Duboin and Lafeuille*, 1992; *Crickmore*, 1994; *Conde and Dyson*, 1995; *Killeen et al.*, 1995; *Niciejewski et al.*, 1996; *Buonsanto and Witasse*, 1999; *Kawamura et al.*, 2000; *Aruliah and Griffin*, 2001]. *Fejer et al.* [2000] and *Emmert et al.* [2001] used daytime upper thermospheric wind measurements from WINDII to study average storm-induced wind perturbations at mid- and low latitudes as a function of magnetic activity, latitude, local time, season, and solar activity. *Emmert et al.* [2002] extended the analysis of daytime WINDII data to lower altitudes, characterizing the seasonal and height dependence of the wind patterns, and also investigated the average time-dependent evolution of the disturbance winds. *Richmond et al.* [2003] analyzed daytime WINDII data near 140 km at high magnetic latitudes to obtain statistical wind patterns for different interplanetary magnetic field (IMF) conditions. *Fejer et al.* [2002] analyzed extensive ground-based wind measurements from Millstone Hill (43°N, 72°W) to investigate the behavior of midlatitude nighttime upper thermospheric winds during storms, finding a complex dependence on season and solar cycle. *Emmert et al.* [2004] studied the behavior of low- to midlatitude nighttime upper thermospheric WINDII observations, which are less extensive than the daytime measurements. *Meriwether* [2008] reviewed storm effects on mid- and low-latitude wind measurements.

[6] Building on these earlier studies, we have developed a global empirical disturbance wind model (DWM07) on the basis of data from WINDII, the DE 2 Wind and Temperature Spectrometer (WATS) [*Spencer et al.*, 1981], and various ground based Fabry-Perot interferometers (FPIs). DWM07 represents the average difference between disturbed and quiet time winds in the upper thermosphere as a function of magnetic latitude, magnetic local time, and the 3-h Kp geomagnetic activity index. In this paper, "perturbation wind" and "disturbance wind" both refer to the difference between the measured wind and the quiet time reference average. DWM07 is the storm time thermospheric component of the new Horizontal Wind Model (HWM07), which is described in a companion paper [*Drob et al.*, 2008]. We consider these models to be provisional because of noted limitations; substantial improvements are under development and will be implemented in the future.

[7] The separation of thermospheric wind patterns into quiet and disturbed components provides several practical advantages. First, it can reduce measurement bias associated with instrument configuration. For example, the upper

thermospheric WINDII data contain offsets related to spacecraft orientation (north- or south-looking) [*Emmert et al.*, 2001]. By including this parameter in the calculation of quiet time reference averages, this bias becomes negligible in the resulting perturbation values. Second, the use of perturbation winds reduces bias between instruments, so that data sets can be more effectively combined to analyze storm effects. As shown in section 5, the disturbance winds obtained from various instruments are generally in good agreement. Finally, the use of perturbation wind data mitigates problems caused by uneven sampling. For example, once the first-order effects of season are subtracted from a data set, one may combine the perturbation winds from all seasons to estimate the seasonally averaged storm effect, even if the seasonal distribution of the data is uneven or dependent on the level of storm activity.

[8] In section 2 we describe the data we used to construct the model and outline our computations of perturbation winds. Sections 3 and 4 detail the formulation of the model, highlight important aspects of its development, and describe the incorporation of DWM07 into HWM07. In section 5 we validate that the model is correctly representing the constituent data, by comparing model profiles with corresponding binned averages from the constituent data sets. We thereby identify discrepancies among the underlying data, and assess how well the model handles these discrepancies. Sections 6 and 7 outline future improvements and summarize our results.

2. Data and Methodology

[9] We used thermospheric wind measurements from UARS WINDII, DE 2 WATS, and seven ground-based FPI stations.

[10] UARS operated in a circular, 57° inclination orbit at a height of 585 km. WINDII is a Michelson interferometer that measured neutral winds between 90 and 300 km via Doppler shifts in the 557.7 nm and 630.0 nm airglow emissions. Details of the WINDII instrument, its observing geometry, and sampling characteristics are given by *Shepherd et al.* [1993] and *Fejer et al.* [2000]. For DWM07, we used 225–275 km measurements from the version 5.11 data set, which covers the period from November 1991 to August 1997. The data and computation of perturbation winds are the same as those used by *Emmert et al.* [2004]. Briefly, we first obtained a quiet time baseline by averaging $Kp < 3$ winds along the UARS orbit, treating different seasons and measurement configurations separately. After subtracting this baseline from all data, we rotated the residual vector winds to magnetic directions, and computed a secondary quiet time baseline as a function of magnetic latitude and local time, season, and solar activity. Finally, we subtracted out this secondary baseline and averaged the 225–275 km residuals over height. Quiet time local time, latitudinal, seasonal, and solar cycle effects were thereby removed from the data.

[11] DE 2 operated from August 1981 to February 1983 in an elliptical polar orbit with initial perigee and apogee heights of 300 km and 1000 km, respectively. WATS [*Spencer et al.*, 1981] was a neutral mass spectrometer that measured in situ cross-track (zonal) winds. We used the Unified Abstract (UA) data set of 16 s averages, which is

available at http://atmoweb.gsfc.nasa.gov. We restricted our analysis to wind measurements between 200 and 600 km, obtaining perturbation winds in a fashion similar to the computation of WINDII perturbation winds, as follows. We first computed a quiet time baseline by averaging the $Kp < 3$ winds along the orbit in $10°$ bins; with the polar orbit this is the same as averaging in latitude bins but treating ascending and descending passes separately. We computed different baselines for each of 24 local time bins, treating data before and after April 1982 separately. Explicit seasonal binning is not necessary, since local time and season covary as a result of the polar orbit. From the quiet time residuals, we computed a secondary correction as a function of magnetic latitude ($10°$ bins) and magnetic local time (24-h bins). The combined baseline was then subtracted from all the data to obtain the set of perturbation winds. Because the geographic northward component is not available from WATS, the residual winds cannot be transformed into magnetic coordinate components. However, in fitting the model, we took the component of the of the vector basis functions along the geographic zonal direction, so that the WATS data influences both the magnetic northward and magnetic eastward components of the model.

[12] We used data from seven ground-based FPI stations: South Pole ($90°S$), Halley ($76°S$, $27°W$), Arequipa ($17°S$, $72°W$), Arecibo ($18°N$, $67°W$), Millstone Hill ($43°N$, $72°W$), Søndre Strømfjord ($67°N$, $51°W$), and Thule ($77°N$, $68°W$). These instruments measured nighttime winds near a height of 250 km via Doppler shifts in the 630.0 nm airglow. Details of each instrument, data reduction methods, and data coverage are given by *Emmert et al.* [2006a] and references therein. For DWM07, we used the same data as that used by *Emmert et al.* [2006a], except that we analyze both quiet time ($Kp < 3$) and disturbed ($Kp \geq 3$) data. We used the station-specific quiet time models developed by *Emmert et al.* [2006a] as the reference baselines for computing perturbation winds.

[13] The WINDII data consist primarily of daytime measurements up to $72°$ geographic latitude, with a smaller number of nighttime measurements below $45°$. The WATS measurements are daytime and nighttime, and are slightly concentrated at high latitudes: 55% of the data are above $55°$. The WATS and nighttime FPI measurements therefore shore up the WINDII coverage, particularly at mid- and high latitudes. Overall, we employed 415,000 WINDII vector wind measurements, 350,000 WATS zonal wind measurements, and 380,000 FPI zonal and meridional wind measurements. The daytime WINDII measurements reach up to magnetic latitudes of $88°$ in the southern hemisphere and $82°$ in the northern hemisphere; at the highest latitudes all magnetic local times are covered except within 2 h of 0000 magnetic local time (MLT). On the other hand, the ground-based FPI winds at the four high-latitude stations include nighttime measurements at all magnetic local times. Therefore, summer high-latitude disturbance winds are primarily represented by WINDII observations, winter high-latitude disturbance winds are primarily represented by the ground-based FPI measurements, and DE 2 provides additional high-latitude measurements in both seasons. In DWM07, which has no seasonal dependence, the summer and winter high-latitude patterns are averaged together. As

shown below, the high-latitude WINDII/summer disturbance winds are similar to the corresponding FPI/winter disturbance winds.

3. Model Formulation

[14] We used vector spherical harmonic (VSH) functions [e.g., *Morse and Feshbach*, 1953; *Swarztrauber*, 1993] to represent the magnetic latitude and local time dependence of the average disturbance winds. Quasi-Dipole (QD) coordinates [*Richmond*, 1995] computed at a static epoch and height of 1994.0/250 km were used for the magnetic coordinate system. The mid- and high-latitude disturbance winds are considerably better organized in magnetic local time and latitude than in geographic latitude and local solar time; fitting in magnetic coordinates greatly reduces the need to include longitude terms in the model. At low latitudes, the relative merits of magnetic versus geographic coordinates are less clear.

[15] We found that the data coverage supports a model resolution of degree 10 in magnetic latitude and order 3 in magnetic local time. The use of higher resolutions introduces spurious variations in the model, particularly under strong geomagnetic activity conditions, when data are sparse.

[16] The disturbance wind patterns include strong latitudinal gradients at the equatorward edge of the high-latitude convection patterns. Representing these gradients with harmonic functions is challenging. The most severe gradients are observed in the zonal winds in the evening sector, as shown in Figure 1 (top). The circles show average WINDII zonal disturbance winds in this sector; the latitudinal profile is characterized by strong and sharp westward jets centered near $65°$, with relatively flat and weakly westward winds at low and midlatitudes. A fit of the averages to Legendre functions up to degree 10 results in the red curve, which contains undesirable oscillations in the flat part of the profile. These oscillations reflect the inability of a truncated harmonic expansion to adequately represent the observed latitudinal profile; the problem is reminiscent of a truncated Fourier representation of a square wave. Spurious oscillations also occur when fitting meridional winds in the morning sector, as shown in Figure 1 (bottom).

[17] Reducing the spurious oscillations by increasing the latitudinal resolution would require truncating at degrees higher than 16, which is not practical given the sparseness of data under strongly disturbed conditions. As an alternative, we found that suppressing the higher-order terms at low and midlatitudes is an effective way to obtain a more robust fit. The dotted lines in Figure 1 show a latitude-dependent weighting function (see equation (1) below) that we applied to Legendre functions of degree 5 and higher. The blue curve shows the resulting fit. The low- and midlatitude oscillations are eliminated, and the model is additionally better able to represent the peaks of the evening westward jets, because the high-degree terms are now focused on this region. The price of this improvement is a loss of the orthogonality of the basis functions, but this is acceptable, because we are only interested in representing the data rather than interpreting the model parameters in terms of oscillatory modes.
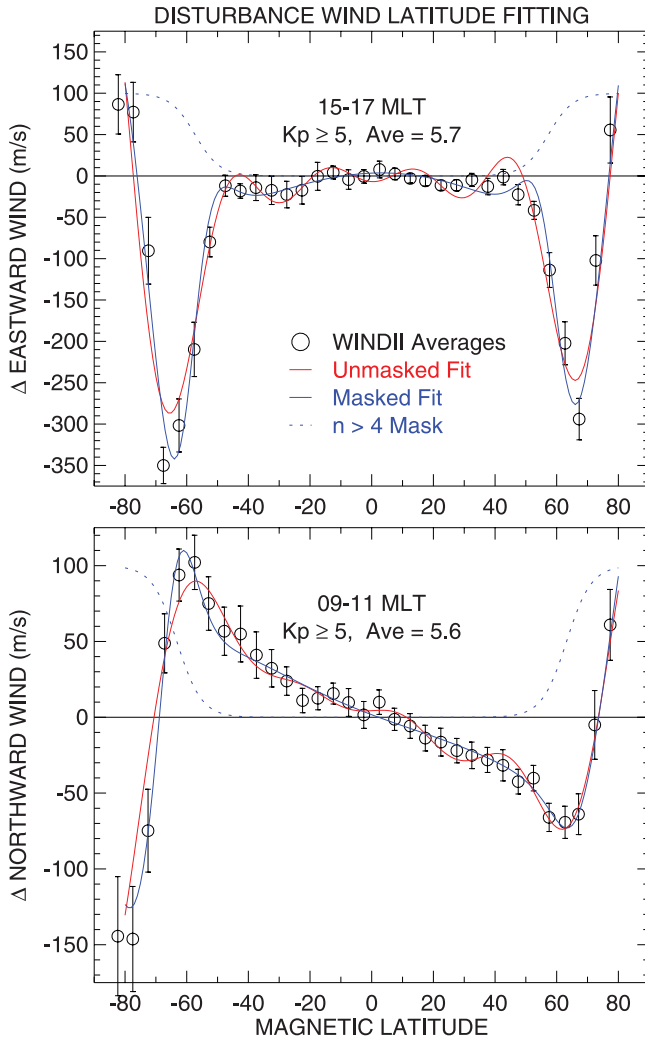
Figure 1. Average WINDII (top) zonal and (bottom) meridional disturbance winds as a function of magnetic latitude in the indicated local time sectors; data corresponding to $Kp \geq 5$ were used in the generation of the plots. The circles show averages in $5°$ bins; error bars indicate the estimated uncertainty of the mean. The red curve shows a fit of the averages to Legendre functions up to degree $n_{max} = 10$. The blue curve shows a fit using the same representation but with the $n > 4$ functions suppressed at low and midlatitudes using the weighting function indicated by the dotted line. See text for details of the weighting function.

[18] The latitude-dependent weighting function is an exponential step function given by

$$w(\lambda; \lambda_t) = \left[1 + \exp\left(\frac{|\lambda| - \lambda_t}{\sigma} \right) \right]^{-1}, \quad (1)$$

where λ is the magnetic latitude, λ_t is the transition latitude, and $\sigma = 4°$ is the transition width. Since the location of strong disturbance wind gradients depends on local time and magnetic activity, we developed the following functional representation of the transition latitude:

$$\lambda_t(\tau, Kp) = a_0 + a_1 \cos \omega\tau + a_2 \sin \omega\tau + \\ Kp(a_3 + a_4 \cos \omega\tau + a_5 \sin \omega\tau), \quad (2)$$
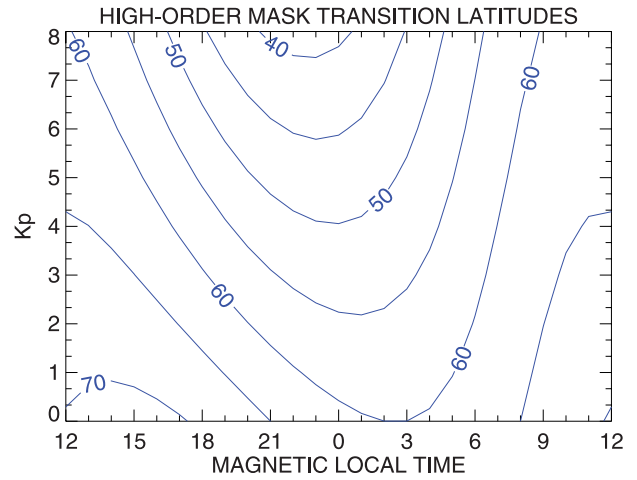

Figure 2. Transition latitudes, as a function of magnetic local time and Kp, used in DWM07 to suppress higher-order latitudinal variations at low and midlatitudes. These latitudes are used with equation (1) to generate a latitude-dependent weighting function for the $n > 4$ model terms.

where τ is the magnetic local time in hours, $\omega = 2\pi/24 \text{ h}^{-1}$, and Kp is the 3-h magnetic activity index. To determine the coefficients a_0, a_1, ..., a_5, we first computed a latitude-local-time-Kp model described by equation (3) below, but without the latitude weighting function. We then evaluated this model on a grid of integer local times and Kp values (from 2 to 8). For each grid point we located the maximum latitudinal gradients in the zonal winds in each hemisphere and fitted the corresponding latitudes (combining hemispheres) to equation (2). The resulting coefficients are $\{65.76, -4.60, -3.54, -2.00, -0.75, 0.97\}$. Figure 2 shows the transition latitude as a function of magnetic local time and Kp.

[19] To represent the dependence of the disturbance winds on the level of magnetic activity, we used three quadratic B-spline functions of the 3-h Kp index, with nodes at $Kp = \{0, 2, 5, 8\}$; these functions are shown in Figure 3. This normalized spline basis is constructed so as to have zero slope at $Kp = 0$ and 8. These constraints
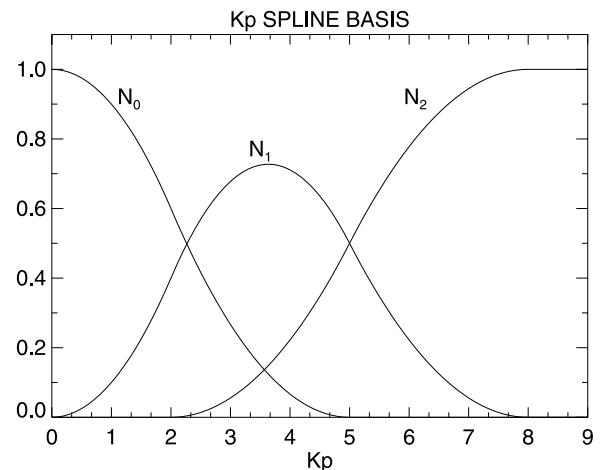

Figure 3. Quadratic B-splines used to represent the Kp dependence of DWM07.

provide needed robustness at the edges of the Kp domain, particularly at the high end, where data are very sparse. Additionally, the last function is extended at a constant level for Kp values higher than 8; the zero slope constraint provides a smooth transition into this region, where data are insufficient to reliably determine the Kp dependence. Although the ap index was used by $Hedin\ et\ al.$ [1988] to represent magnetic activity effects in the earlier HWMs, we found that the disturbance winds tend to have a more linear dependence on Kp than on ap, and are therefore easier to represent empirically with Kp. The number of nodes and their locations were selected to give a robust representation of the data at the highest practical resolution (following the fitting strategies outlined by $Emmert\ et\ al.$ [2006a]). The model results are insensitive to small (<1) changes in the interior node locations.

[20] The complete model formulation is given by

$$\Delta \vec{U}(\lambda, \tau, Kp) = \sum_{k=0}^{2} \sum_{n=0}^{4} \sum_{m=0}^{3} N_k(Kp)\vec{A}_{knm}(\lambda, \tau)$$
$$+ \sum_{k=1}^{2} \sum_{n=5}^{10} \sum_{m=0}^{3} N_k(Kp)\vec{A}_{knm}(\lambda, \tau)w(\lambda; \lambda_t(\tau, Kp)),$$

$$(3)$$

where N_k are the Kp splines shown in Figure 3, and

$$\vec{A}_{knm} = b_{knm}^R \vec{B}_{nm}^R + b_{knm}^I \vec{B}_{nm}^I + c_{knm}^R \vec{C}_{nm}^R + c_{knm}^I \vec{C}_{nm}^I; \quad (4)$$

$$\vec{B}_{nm}^R = \left[+ \frac{d\overline{P}_{nm}}{d\theta} \cos(m\omega\tau)\hat{e}_\theta - \frac{m}{\sin\theta} \overline{P}_{nm} \sin(m\omega\tau)\hat{e}_\phi \right] \frac{1}{\sqrt{n(n+1)}}$$
$$\vec{B}_{nm}^I = \left[- \frac{d\overline{P}_{nm}}{d\theta} \sin(m\omega\tau)\hat{e}_\theta - \frac{m}{\sin\theta} \overline{P}_{nm} \cos(m\omega\tau)\hat{e}_\phi \right] \frac{1}{\sqrt{n(n+1)}}$$
$$\vec{C}_{nm}^R = \left[- \frac{m}{\sin\theta} \overline{P}_{nm} \sin(m\omega\tau)\hat{e}_\theta - \frac{d\overline{P}_{nm}}{d\theta} \cos(m\omega\tau)\hat{e}_\phi \right] \frac{1}{\sqrt{n(n+1)}}$$
$$\vec{C}_{nm}^I = \left[- \frac{m}{\sin\theta} \overline{P}_{nm} \cos(m\omega\tau)\hat{e}_\theta + \frac{d\overline{P}_{nm}}{d\theta} \sin(m\omega\tau)\hat{e}_\phi \right] \frac{1}{\sqrt{n(n+1)}}$$

$$(5)$$

$$\overline{P}_{nm}(\theta) = \sqrt{\frac{(2n+1)(n-m)!}{2(n+m)!}} P_{nm}(\theta); \quad (6)$$

$$\theta = \pi/2 - \lambda; \quad (7)$$

$P_{nm}(\theta)$ and $\overline{P}_{nm}(\theta)$ are, respectively, the unnormalized and normalized associated Legendre functions; and $\hat{e}_\theta$ and $\hat{e}_\phi$ are respectively the southward and eastward unit vectors. The functions $dP_{nm}/d\theta$ and $mP_{nm}/\sin\theta$ (which are related to the gradients of scalar spherical harmonics) are defined at all latitudes and can be computed using standard recursion relations [e.g., $Holmes\ and\ Featherstone$, 2002]. The four vector functions $\vec{B}^R$, $\vec{B}^I$, $\vec{C}^R$, $\vec{C}^I$ are the real and imaginary

parts of the irrotational (B) and solenoidal (C) complex VSH functions. In equation (3), the $m > n$ VSH functions are zero, as are the $(n, m) = (0,0)$ function and the imaginary part of the $m = 0$ functions. Consequently, 128 nonzero VSH functions multiply the three Kp splines. The higher-degree VSH functions are not used under quiet conditions, so the first Kp spline only multiplies the $n \leq 4$ VSH functions. The latitude weighting function is applied to the $n > 4$ VSH functions. This gives a total of 300 linear terms in the model, plus the 6 terms that describe the transition latitude of the weighting function w.

[21] To compute the model terms $\{b_R, b_I, c_R, c_I\}_{knm}$, we minimized the sum of squared differences between the line of sight wind measurements and the corresponding model component. The WINDII data and some of the FPI data are vector observations, of which the zonal and meridional components were treated as separate line of sight winds. These data records consequently get twice the weight of the DE 2 WATS records, which only consist of one wind component.

4. Incorporation Into HWM07

[22] The model represents height-averaged disturbance winds above 225 km. $Emmert\ et\ al.$ [2002] showed that average disturbance winds are roughly independent of height above a cutoff at $\sim$120 km, but that there are some important height effects. In order to incorporate DWM07 into the height-dependent HWM07, we apply an artificial height profile that extends DWM07 downward to 125 km, at which height an exponential step function smoothly zeros out the disturbance winds. The transition function is given by

$$h(z) = \left[1 + \exp\left(\frac{z - z_t}{\sigma}\right) \right]^{-1}, \quad (8)$$

where z_t = 125 km is the transition height and σ = 5 km is the transition width. Figure 4 shows examples of WINDII average disturbance wind profiles along with artificial profiles applied to the average values near 250 km. In many cases, the improvised height dependence reasonably mimics the height dependence of the observed winds. However, it misses features like the reversal from westward to eastward perturbations in the 0600–0900 MLT sector, the maximum westward disturbance near 150 km in the 1500–1800 MLT sector, and significant meridional disturbances down to 110 km in the 0600–0900 MLT sector. A more realistic representation of the height dependence is clearly needed.

[23] To add the DWM07 perturbation winds to HWM07, which represents quiet time winds in geographic coordinates, we evaluate DWM07 for the magnetic latitude, local time, and magnetic activity corresponding to the HWM07 input arguments. We then apply the artificial height variation, obtain the geographic east and north components (following $Richmond\ et\ al.$ [2003]) of the resulting vector disturbance wind, and add the results to the corresponding HWM07 quiet time wind components.

[24] One of the advantages of using VSH functions to represent a vector field is that they properly account for
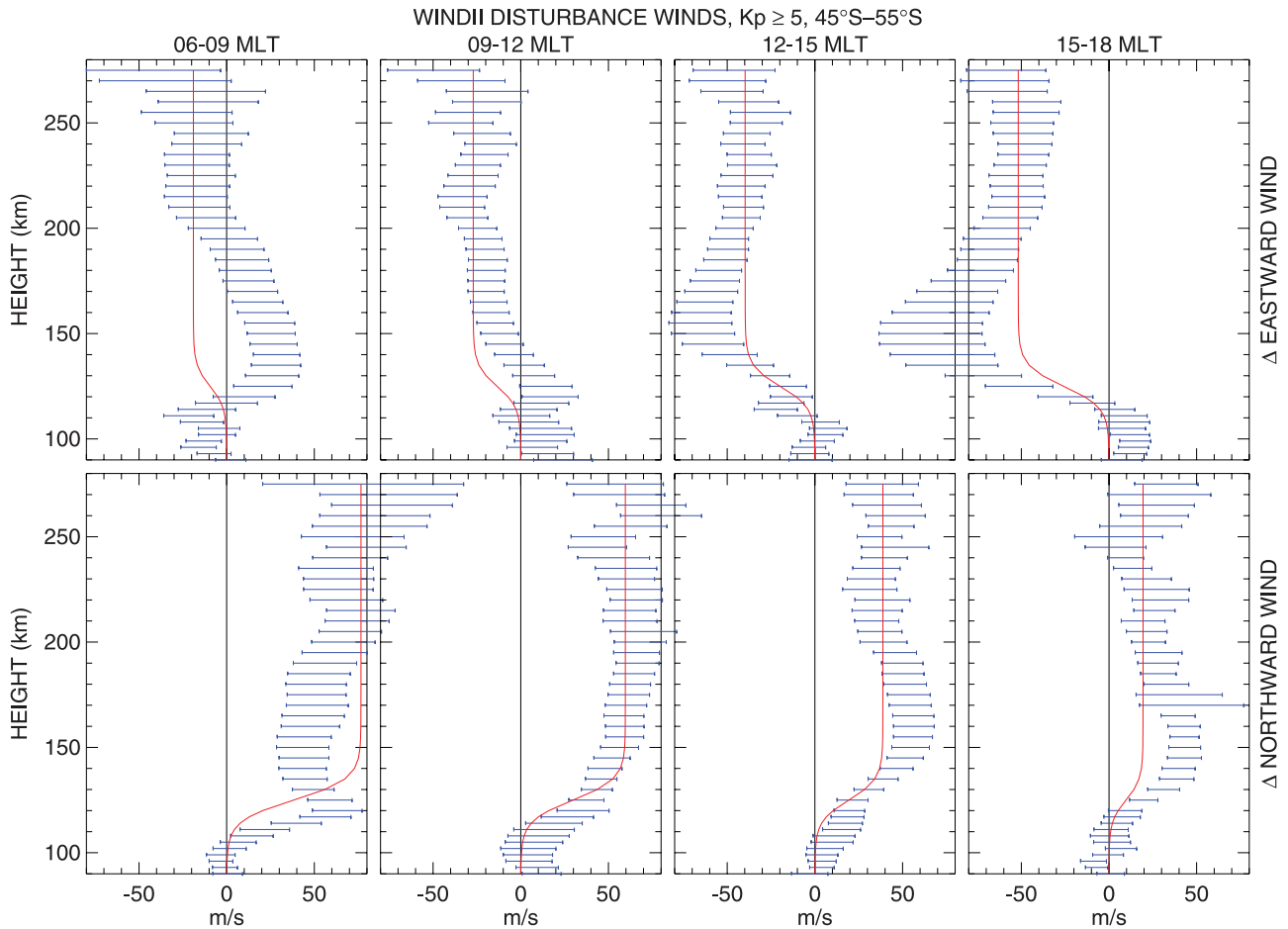
Figure 4. Average WINDII (top) zonal and (bottom) meridional disturbance winds as a function of height (blue horizontal bars); the width of the bars indicates the estimated uncertainty of the mean. $Kp \geq 5$ data between 45 and 55°S magnetic latitude, and in the indicated magnetic local time sectors, were used to compute the averages. The red curves show the artificial extension of the $225-275$ average disturbance winds to lower altitudes via multiplication by equation (8).

singularities and ambiguities near the poles, thus providing a continuous global representation. An important aspect of a vector field on a sphere is that even though the azimuthal coordinate is degenerate at the poles, it still serves to define the orientation of a vector at the pole, as shown in Figure 5. Slightly off the north pole along longitude (or local time) ϕ, the basis vectors are unambiguously defined. Moving up to the pole along this meridian, the orientation of the basis vectors should not change. Therefore, at the pole, the "eastward" component ($\hat{e}_\phi$) points to the $\phi + \pi/2$ meridian, and the "northward" component ($-\hat{e}_\theta$) points to the opposite meridian from ϕ. The situation is the same in the southern hemisphere, except that the northward component points to the selected meridian instead of the opposite meridian.

[25] In DWM07 the magnetic eastward and magnetic northward basis vectors are oriented according to the magnetic local time input. At a magnetic pole, the computation of magnetic longitude and local time from the HWM07 input arguments (UT, geographic longitude, and
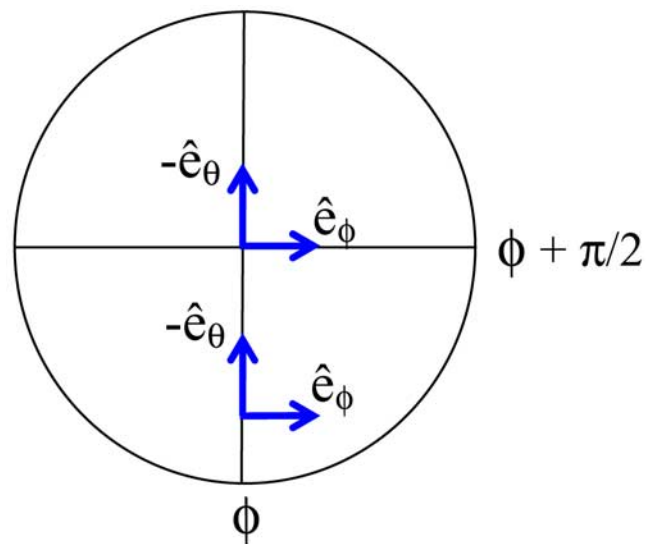

Figure 5. Schematic diagram showing how the azimuthal coordinate defines the orientation of the zonal and meridional unit vectors at the poles of a spherical coordinate system. See text for details.
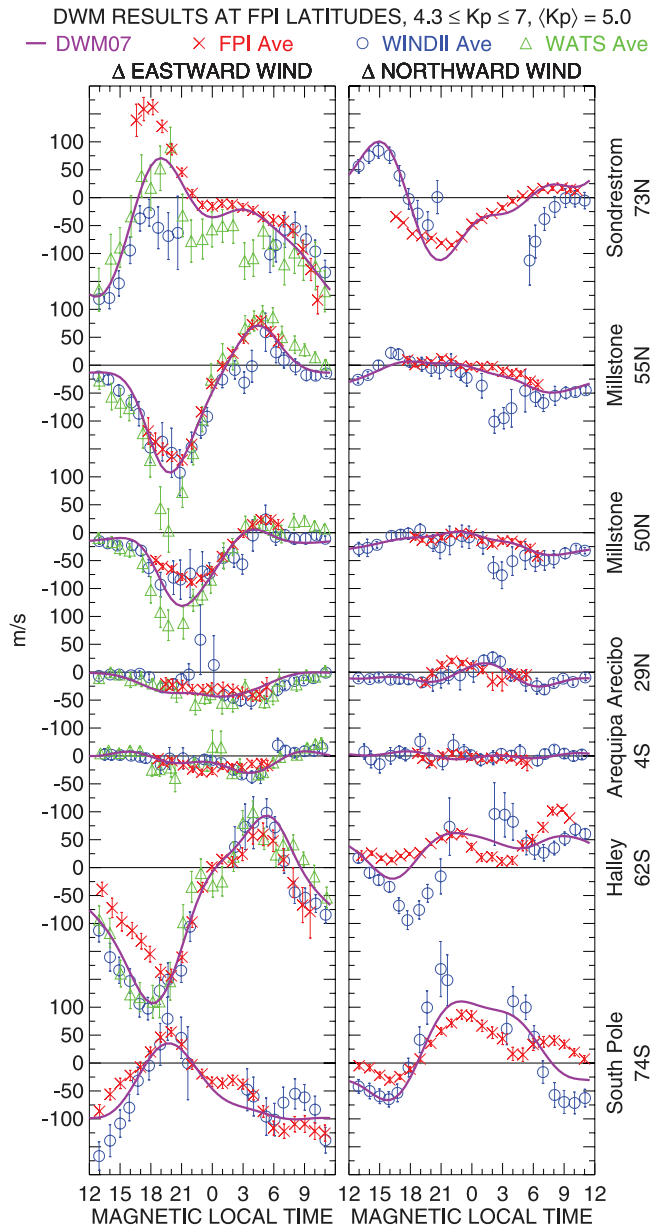
Figure 6. Average (left) zonal and (right) meridional disturbance winds computed from ground-based FPI data (red crosses), UARS/WINDII data (blue circles), and DE 2/WATS data (green triangles) as a function of magnetic local time (2-h bins at 1-h intervals). Data corresponding to $4.3 \leq Kp \leq 7.0$ were used to compute the averages. Error bars denote the estimated uncertainty of the mean. WINDII and WATS data within $4°$ of the magnetic latitude of each FPI station were used to compute the averages. The purple curve shows corresponding results from DWM07. The wind components refer the magnetic eastward and magnetic northward directions, except for the WATS results, which are longitudinally averaged geographic eastward disturbance winds.

geographic latitude) produces arbitrary but mutually consistent values. The obtained magnetic longitude value must be used in the computation of the geographic components of

the perturbation wind vector; otherwise, the components will not be compatible with the HWM07 input arguments.

5. Model Results and Discussion

[26] In this section we compare DWM07 predictions with its constituent data. We thereby validate that the model adequately represents (within the limits of its resolution) average variations evident in the data, that it does not overfit the data, and that it behaves robustly where data are sparse. We also identify discrepancies among the data sets and assess how the model handles them.

5.1. Local Time Dependence

[27] Figure 6 shows DWM07 results as a function of magnetic local time at the magnetic latitudes of the FPI stations. Corresponding binned average disturbance winds from WINDII, WATS, and the FPIs are also shown. North- and south-looking Millstone Hill results, which are separated by $\sim 5°$, are shown separately. The comparison of WINDII and FPI data with WATS data is not ideal: The meridional component is not available, so the WATS values represent the longitudinally averaged geographic eastward disturbance winds (in magnetic latitude bins), whereas the other values in Figure 6 denote the average magnetic eastward disturbance winds. However, we do not expect that this difference in data processing significantly affects the longitudinally averaged winds, as long as the latitudinal bin is equatorward of both the geographic and magnetic poles. Note that this issue is relevant only to the binned averages, not the model results; the direction of the WATS measurements was properly accounted for in the model assimilation process.

[28] The zonal disturbance winds from the three databases are in good agreement at mid- and low latitudes, and the model represents their MLT variation well. At Millstone Hill the WATS westward disturbances around 2000 MLT are stronger than those of the other data sets; DWM07 tends somewhat toward these larger values. It is likely that solar cycle (solar maximum for WATS) and altitudinal (higher for WATS) sampling differences are contributing to the larger observed westward disturbance winds: Under winter conditions, evening westward disturbance winds over Millstone Hill are strongest at solar maximum [*Fejer et al.*, 2002].

[29] At the magnetic latitude of Halley the FPI, WINDII, and WATS zonal winds are in good agreement, although the westward disturbance winds around 1800 MLT are 50 m/s stronger in the case of WINDII and WATS; DWM07 closely follows these data. At South Pole, the WINDII zonal disturbance winds are similarly about 50 m/s stronger than the FPI averages in the 1200–1600 MLT sector, and about 50 m/s weaker near 0800 MLT, but are otherwise in good agreement. Differences in the dusk sector are more pronounced at Søndre Strømfjord, where the average FPI, WATS, and WINDII disturbance winds are 150 m/s eastward, 50 m/s eastward, and 50 m/s westward, respectively. The differences between the high-latitude WINDII and FPI results could be attributable to seasonal differences in high-latitude convection patterns, given that the WINDII data are entirely daytime/summer, whereas the FPI data are nighttime/winter. The WATS data represent a mix of summer and winter conditions in this MLT sector. At Søndre
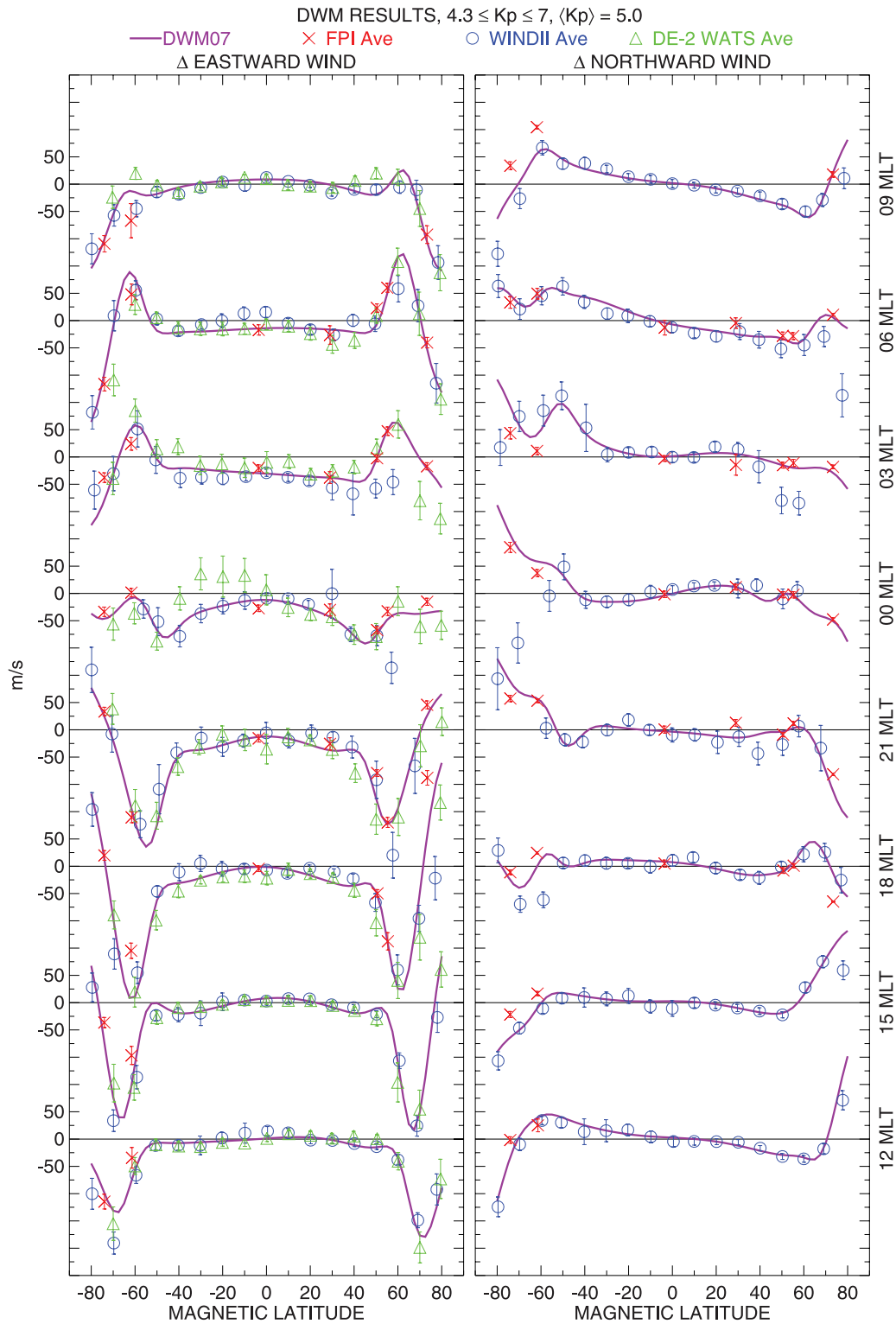
Figure 7. Average (left) zonal and (right) meridional disturbance winds computed from ground-based FPI data (red crosses), UARS/WINDII data (blue circles), and DE 2/WATS data (green triangles) as a function of magnetic latitude (10° bins in the case of the satellite data). Data in 2-h magnetic local time bins and corresponding to $4.3 \leq Kp \leq 7.0$ were used to compute the averages. Error bars denote the estimated uncertainty of the mean. The purple curve shows corresponding results from DWM07.

Strømfjord, DWM07 follows WINDII data on the sunward side and FPI data on the nightside; in the discrepant region of overlap near 1800 MLT, DWM07 roughly follows the WATS data. DWM07 follows the WINDII and WATS data over Halley, and over South Pole it follows an average of the WINDII and FPI patterns.

[30] The high-latitude FPI and WINDII meridional disturbance winds shown in Figure 6 (right) show several noticeable discrepancies. At Søndre Strømfjord the dayside WINDII disturbances and the nightside FPI disturbance form a reasonably continuous local time dependence, although the WINDII data near 0600 MLT veer equatorward. At Halley there is no clear consistency between the FPI and WINDII data, except that both show equatorward disturbances on the order of 50 m/s in the 0300–1200 MLT sector. The WINDII and South Pole FPI averages show a clearer consistency of overall pattern (poleward winds from 1200 to 1800 MLT and equatorward winds from 1800 to 0600 MLT), but the pattern of differences is similar to that of the Halley-WINDII differences: The FPI disturbance winds are generally more northward from 0600 to 1800 MLT, and more southward from 2100 to 0600 MLT. In addition to the seasonal sampling differences between the WINDII and FPI high-latitude data, there are longitudinal sampling differences that may also contribute to the meridional disturbance wind discrepancies: Within 4° of Halley's magnetic latitude of 62°S, WINDII samples all geographic longitudes except 90°W–10°W, thus excluding Halley's longitude of 27°W. Within 4° of South Pole's magnetic latitude of 74°S, WINDII only samples geographic longitudes from 40°E eastward to 160°W, and geographic latitudes from 55°S to 72°S; the centers of the WINDII and South Pole sampling regions are thus geographically separated by about 25°.

[31] At Millstone Hill the WINDII and FPI meridional wind data are in good agreement except in the 0100–0400 MLT sector, where the WINDII perturbations are up to 75 m/s more equatorward than the FPI perturbations. In this case, both data sets consist of nighttime, seasonally averaged data, so seasonal effects are not a likely cause of the discrepancy. Furthermore, the WINDII data at these magnetic latitudes are concentrated in the 120°W–30W° longitude sector (the nighttime WINDII data are confined to geographic latitudes below 45°), so the FPI and WINDII longitude sampling is similar. It may not be possible to satisfactorily resolve this discrepancy with the existing data, given that the amount of WINDII data is very small (114 observations in the 0100–0400 MLT sector contributed to the 55°N WINDII averages shown in Figure 6). The issue is further complicated by the complex seasonal and solar cycle dependence of meridional disturbance winds over Millstone Hill [*Fejer et al.*, 2002]. DWM07 follows the pattern of the more extensive FPI data.

[32] At Arecibo both the WINDII and FPI data show small equatorward disturbances near dawn and dusk, as well as small poleward perturbations during the night. However, the WINDII poleward feature occurs 3 h after the FPI feature. DWM07 follows the more extensive WINDII data. At Arequipa, neither the WINDII nor FPI measurements show significant average meridional disturbances. This is expected from symmetry considerations, given Arequipa's location near the equator of our coordinate system and the fact that we have averaged over all seasons.

5.2. Latitude Dependence

[33] Figure 7 shows average FPI, WINDII, and WATS disturbance winds as a function of latitude, in 2-h MLT bins centered on the indicated MLT. There is very good agreement among the zonal disturbance winds from the three data sets, particularly with respect to the location and magnitude of the 1200–0000 MLT westward jets and the postmidnight eastward peaks. The difference between the north-looking and south-looking Millstone Hill FPI data reflects the steep gradients in the zonal disturbance winds near 55°N, and agrees very well with the WINDII and WATS data. DWM07 represents the latitude dependence of the observed average zonal disturbance winds well.

[34] The latitude dependences of the FPI and WINDII meridional disturbance winds are fairly consistent, other than the aforementioned 0300 MLT discrepancy between the Millstone Hill FPI and WINDII data and the lack of consistent agreement between the FPI and WINDII averages at southern high latitudes. The DWM07 nighttime latitude dependence is somewhat noisy at midlatitudes and above, as a result of these discrepancies and the sparseness of meridional wind measurements in this region.

5.3. *Kp* Dependence

[35] Figure 8 shows DWM07 zonal disturbance winds as a function of *Kp*, at the magnetic latitudes of the FPI stations, along with corresponding binned averages of FPI, WINDII, and WATS data. The *Kp* dependences of the three data sets are in very good agreement except at Søndre Strømfjord. The model's imposed saturation at both ends of the *Kp* domain appears to be an appropriate representation of the data under most conditions. Some discontinuities in the slope of the model *Kp* dependence at *Kp* = 8 are noticeable in the plots: Although the quadratic spline basis provides continuity up to the first derivative, the *Kp* dependence of the transition latitude function *w* (equations (1) and (2)) does not, being linear up to *Kp* = 8 and constant for *Kp* > 8.

[36] Figure 9 shows DWM07 meridional disturbance winds as a function of *Kp*. Other than the discrepancies (see section 5.1) between the WINDII and FPI meridional data at Halley and Millstone Hill, the *Kp* dependences of the FPI and WINDII data are in generally in good agreement up to a *Kp* of at least 4 or 5. At higher levels, the two data sets diverge in some cases. At Søndre Strømfjord at 0600 MLT, there are large differences between the FPI and WINDII disturbance winds, but the shapes of the *Kp* curves are similar. The constrained saturation of the model at *Kp* = 8 appears to be an appropriate representation of the data in some cases (e.g., South Pole at 0000 MLT), but in several cases the *Kp* dependence of the data appears to have an increasing slope (e.g., Halley at 0600 MLT). Unfortunately, robustly modeling the slope of the *Kp* dependence under strongly disturbed conditions does not appear to be feasible with currently available data, particularly for the meridional component, which is more difficult to represent climatologically than the zonal component. The saturation constraint provides robustness while still representing the major shifts, associated with increasing magnetic activity, in the disturbance wind data.

5.4. Global Patterns

[37] Figure 10 summarizes the magnetic local time and latitude dependence of the DWM07 meridional and zonal disturbance winds at three *Kp* levels. The patterns are very similar to the *Kp* = 4 patterns computed by *Emmert et al.*
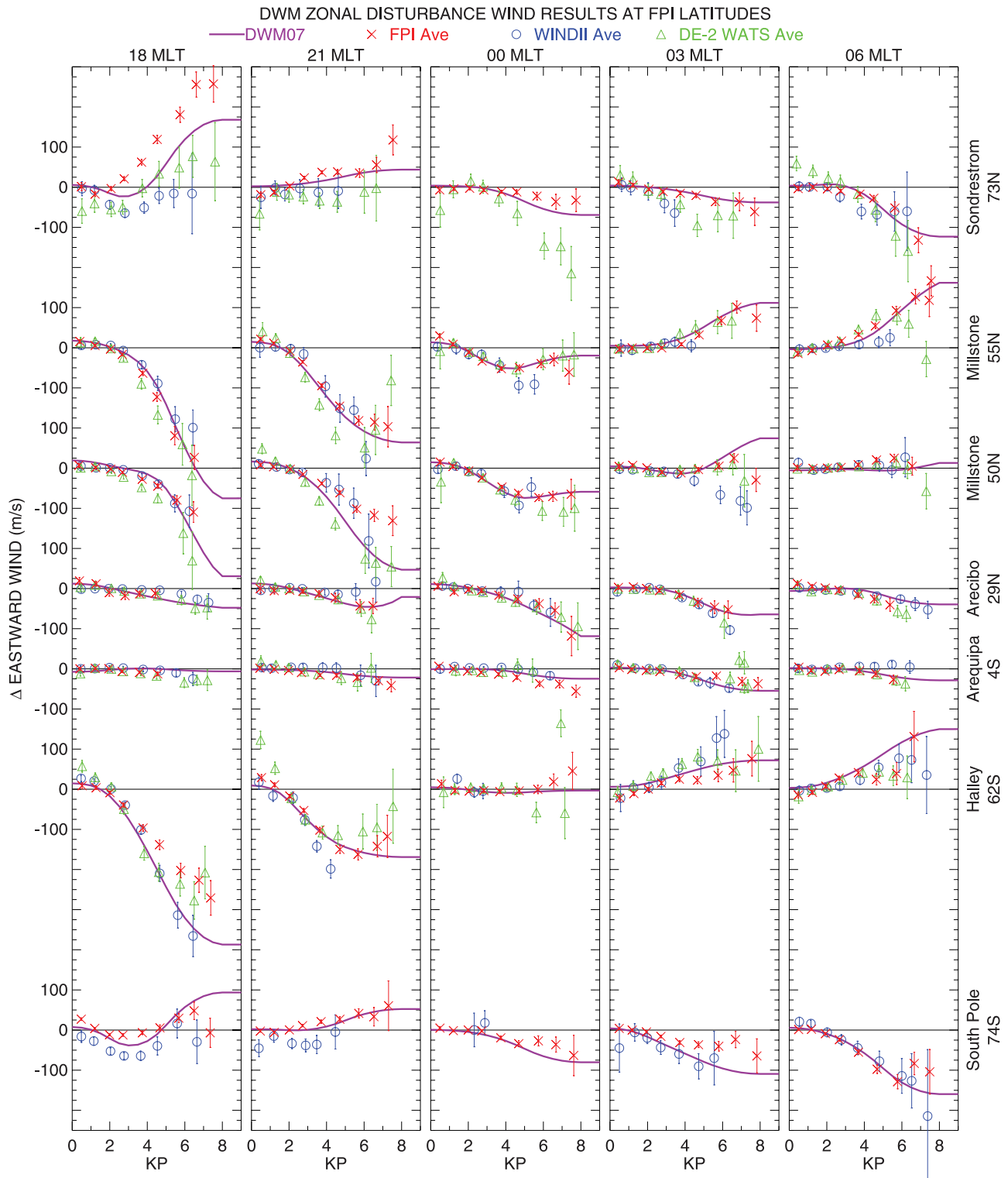
Figure 8. Average zonal disturbance winds computed from ground-based FPI data (red crosses), UARS/WINDII data (blue circles), and DE 2/WATS data (green triangles) as a function of Kp (nine bins: ≤0.7, $0.7-1.7$, $1.3-2.7$, $2-3.7$, $3-5$, $4-6$, $5-8$, $6-9$, and ≥7). Three-hour magnetic local time bins, centered on the indicated times, were used. Satellite data within $4°$ of the magnetic latitude of each FPI station were used. Error bars denote the estimated uncertainty of the mean. The purple curve shows corresponding results from DWM07.
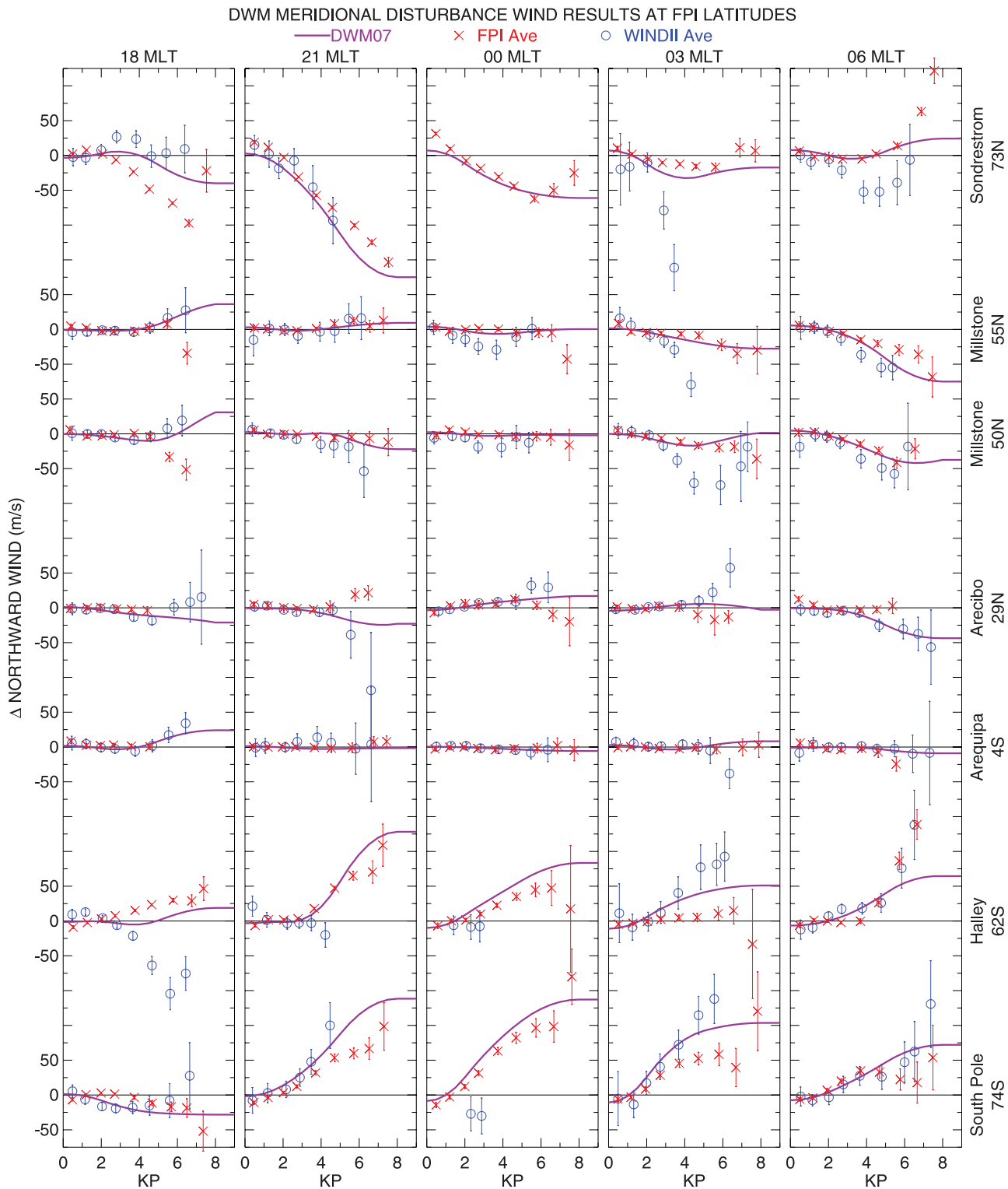
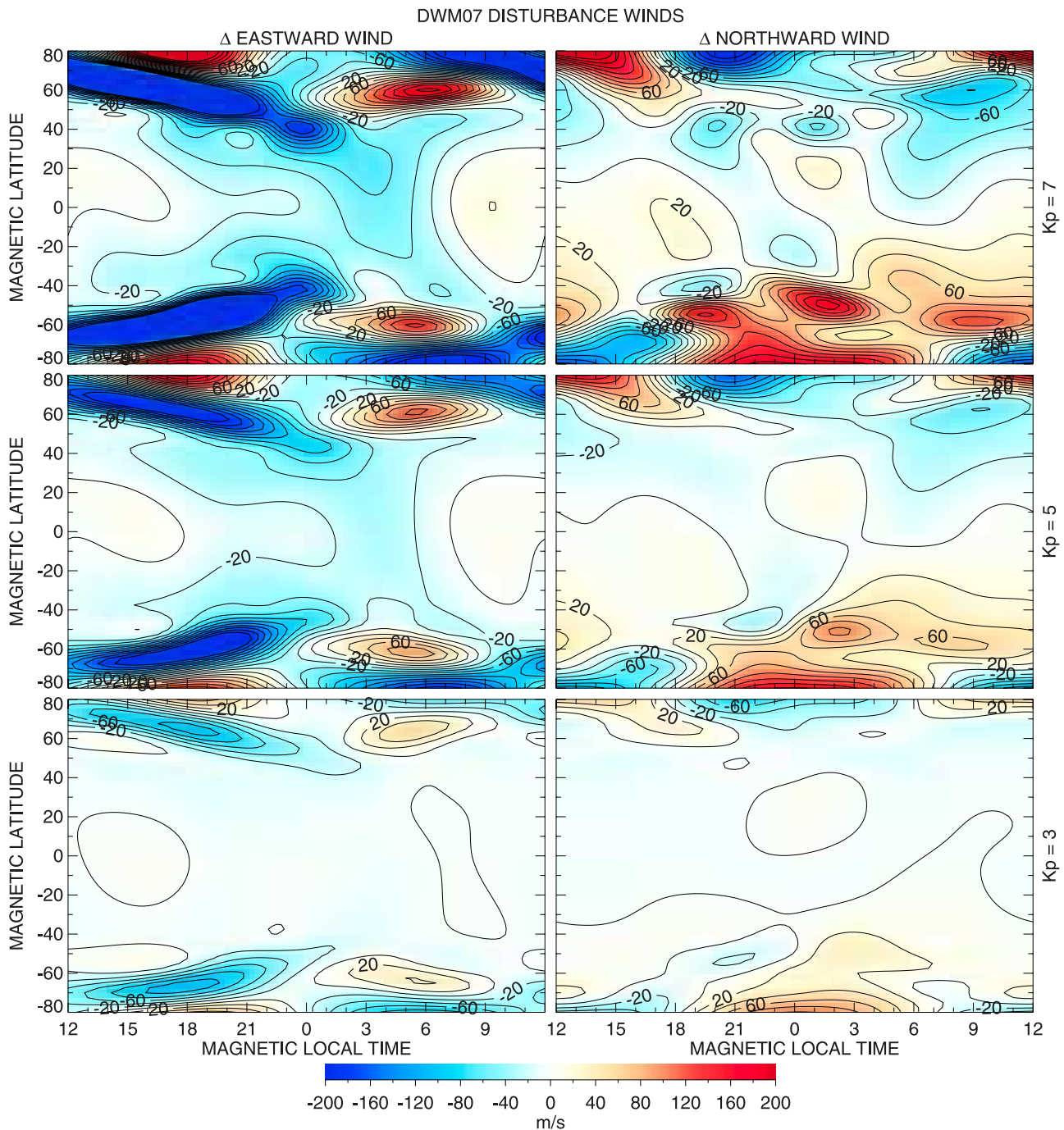**Figure 9.** Same as Figure 8 but for the meridional component.

Figure 10. DWM07 (left) zonal and (right) meridional disturbance winds as a function of magnetic local time and latitude for three different *Kp* levels. The contour interval is 20 m/s, and the maximum contour shown is 200 m/s.

[2004] using WINDII data only, but additionally show the intensification of the disturbance winds and their expansion to lower latitudes with increasing *Kp*.

[38] The DWM07 zonal disturbance wind patterns are hemispherically very symmetric and appear to be well behaved all the way up to *Kp* = 8, the highest level represented by the model. There are areas of eastward disturbances from 0000 to 0900 MLT near 60°, and weak eastward perturbations from 0700 to 1800 MLT below 30°. Otherwise, the disturbances below 70° are westward. The

strong afternoon and evening westward jets at upper mid-latitudes intensify and expand to lower latitudes with increasing *Kp*. At *Kp* = 7, distinct areas of strong westward winds appear at the end of the jets at midnight near 40°.

[39] The meridional disturbance wind patterns below 60° are dominated by equatorward flows, particularly on the dayside. At night the pattern becomes more complicated with increasing *Kp*; at *Kp* = 7 there are relatively strong areas of equatorward winds at 40–50°, and weaker pole-ward areas at lower latitudes. Given the sparseness of
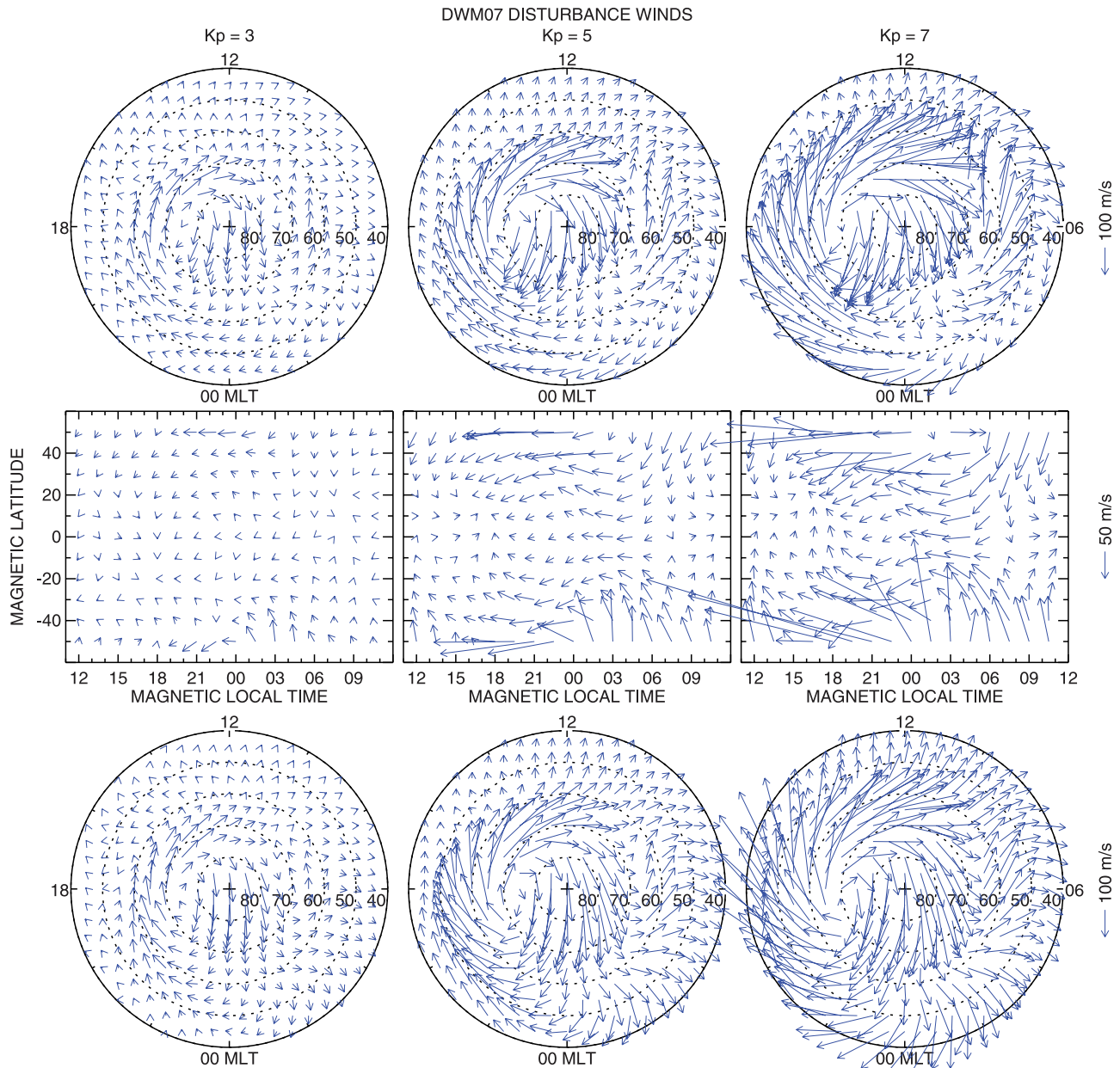
Figure 11. DWM07 vector disturbance winds as a function of magnetic latitude and local time at (top) northern high latitudes, (middle) mid- and low latitudes, and (bottom) southern high latitudes. Results are shown for three different *Kp* levels. Note the different vector magnitude scale at low and midlatitudes.

nighttime high-*Kp* data at these latitudes and the difficulties we encountered in characterizing the meridional wind response under these conditions, these features of the model should be viewed with caution.

[40] Figure 11 shows DWM07 vector wind patterns over the poles and at low and midlatitudes for three different *Kp* levels. The low- and midlatitude patterns are similar to the *Kp* = 4 patterns computed by *Emmert et al.* [2004]. The high-latitude patterns are dominated by a strong duskside anticyclonic convection cell that is clearly associated, via ion drag, with enhanced ion convection under disturbed conditions [*Killeen and Roble*, 1988; *Fejer et al.*, 2002; *Richmond et al.*, 2003]. The dusk cell intensifies and expands dramatically with increasing *Kp*. At *Kp* = 7,

average disturbance winds reach magnitudes in excess of 300 m/s. Average quiet time wind amplitudes at high latitudes are typically 100–200 m/s [*Emmert et al.*, 2006a, 2006b]. Therefore total winds in excess of 500 m/s could be expected, on average, under strongly disturbed conditions. The high-latitude DWM07 patterns also show a narrow but fairly distinct cyclonic dawn cell. This ion-driven feature is not typically observed in quiet time winds because of competing antisunward pressure gradient and Coriolis forces [e.g., *Meriwether et al.*, 1973; *McCormac and Smith*, 1984; *Thayer and Killeen*, 1993].

[41] Around 0000 MLT/60° in both hemispheres, there appears to be a distinct interruption between the enhanced antisunward flows observed at high latitudes and the equa-

torward flows seen at lower latitudes. The statistical significance of this feature is questionable given the difficulties we encountered in characterizing the meridional disturbance winds in this region (see sections 5.1–5.3). On the other hand, if the feature is real then it would indeed be difficult to represent empirically given the limited available data. The apparent wind divergence might be explained by divergent pressure gradients associated with enhanced auroral heating.

[42] The equatorward disturbance winds observed in the mid- and low-latitude 0600–1200 MLT sector, which increase linearly with latitude (Figure 7) [*Fejer et al.*, 2000; *Emmert et al.*, 2001], appear to arise from the convergence of the dusk cell westward winds and the dawn cell eastward winds near 60°. Physics-based model simulations could be used to test this hypothesis. Heating-induced pressure gradients may also contribute to the equatorward flow in this sector.

6. Future Development

[43] The model's representation of disturbance wind patterns would be enhanced with the addition of season, altitude, and solar cycle arguments. At daytime low and midlatitudes, the addition of seasonal terms will have some influence on the daytime disturbance winds, which have a weak winter-to-summer flow in the afternoon [*Emmert et al.*, 2002]. The seasonal dependence of nighttime low- and midlatitude disturbance winds has been difficult to establish from WINDII data because of its sparseness in this sector. The Millstone Hill meridional disturbance wind data show a strong, complex dependence on season and solar cycle, but it will be difficult to robustly incorporate these effects into a global empirical model. The most significant impact of seasonal terms will likely be at high latitudes, where WINDII daytime/summer measurements will essentially be treated separately from FPI nighttime/winter measurements. While this will make it possible for DWM07 to better represent the extant data, a clear picture of the seasonal dependence of high-latitude disturbance winds will require more extensive observational data sets, particularly on the dayside.

[44] The incorporation of height dependence into DWM07 would result in more realistic disturbance winds in the daytime lower thermosphere than our current downward extension of upper thermospheric disturbance winds (section 4). Because of the lack of nighttime wind measurements between 120 and 200 km, accurate empirical representation of average disturbance winds in nighttime lower thermosphere is currently unfeasible, although it may be possible to extrapolate daytime and upper thermospheric estimates into this region.

[45] Solar cycle effects at daytime mid- and low latitudes are generally weak, but the equatorward winds are somewhat stronger during solar minimum than solar maximum [*Emmert et al.*, 2001]. In contrast, nighttime mid- and low-latitude meridional disturbance winds are generally more poleward at solar minimum [*Emmert et al.*, 2004].

[46] The incorporation of the effects of IMF orientation and strength would also enhance the model. A significant dependence on these parameters is likely, given that drag from enhanced ion convection is a major source of the disturbance winds. Systematic IMF orientation effects have been detected in quiet time winds [e.g., *Sica et al.*, 1989; *Emmert et al.*, 2006b] and in total winds under disturbed conditions [e.g., *Hernandez et al.*, 1991].

[47] Finally, a comprehensive empirical model of storm time winds should represent the typical time-dependent evolution of the winds during the onset and recovery of a storm. *Emmert et al.* [2002] investigated the average evolution of daytime mid- and low-latitude winds, finding complex patterns of storm development and recovery. Incorporating these effects into a global empirical model will be very challenging, even if the amount of available data increases substantially.

7. Summary

[48] We developed a global empirical disturbance wind model that represents average geospace-storm-induced perturbations of upper thermospheric neutral winds on the basis of satellite-based data from UARS WINDII and DE 2 WATS, and ground-based data from seven FPI stations. DWM07 depends on three parameters: magnetic latitude, magnetic local time, and the 3-h Kp geomagnetic activity index. The latitude and local time dependence is represented by vector spherical harmonic functions (up to degree 10 in latitude and order 3 in local time), and the Kp dependence is represented by quadratic B-splines. To reduce spurious oscillations induced by strong latitudinal gradients in the data at midlatitudes, the model resolution is truncated at degree 4 below a predetermined transition latitude that depends on local time and Kp.

[49] DWM07 is the storm time thermospheric component of the new Horizontal Wind Model (HWM07), which is presented in a companion paper [*Drob et al.*, 2008]. To incorporate DWM07 into HWM07, we imposed an artificial height profile that extends the upper thermospheric DWM07 perturbation winds down to a smooth cutoff at 125 km.

[50] The perturbation winds derived from the three data sets are in good mutual agreement under most conditions, and the model captures most of the climatological variations evident in the data. There are several discrepancies among the data sets, however; most are at high latitudes and may be attributable to different seasonal and longitudinal sampling. There is also a significant discrepancy between postmidnight midlatitude meridional disturbance winds derived from WINDII measurements and those derived from Millstone Hill FPI measurements; the former are more equatorward by up to 75 m/s on average. Meridional disturbance winds in this sector display a complex dependence on season and solar cycle, and more data is needed to resolve this discrepancy.

[51] The DWM07 disturbance wind patterns at high latitudes include a strong anticyclonic dusk circulation cell and a weak cyclonic dawn cell. Mid- and low-latitude disturbance winds are predominantly westward and equatorward, except for weak eastward flows at daytime low latitudes and some weak poleward flows at nighttime low to midlatitudes. With increasing Kp, the disturbance winds intensify and the high-latitude circulation expands to lower latitudes. Needed improvements to DWM07 include the addition of altitude, season, and solar cycle terms.

References

Aruliah, A. L., and E. Griffin (2001), Evidence of meso-scale structure in the high-latitude thermosphere, *Ann. Geophys.*, 19, 37–46.

Buonsanto, M. J., and O. G. Witasse (1999), An updated climatology of thermospheric neutral winds and F region ion drifts above Millstone Hill, *J. Geophys. Res.*, 104, 24,675–24,687, doi:10.1029/1999JA900345.

Burns, A. G., T. L. Killeen, W. Deng, G. R. Carignan, and R. G. Roble (1995), Geomagnetic storm effects in the low- to middle-latitude upper thermosphere, *J. Geophys. Res.*, 100, 14,673–14,692, doi:10.1029/94JA03232.

Conde, M., and P. L. Dyson (1995), Thermopsheric horizontal winds above Mawson, Antarctica, *Adv. Space Res.*, 16, 41–52, doi:10.1016/0273-1177(95)00171-A.

Crickmore, R. I. (1994), Mean thermospheric winds observed from Halley, Antarctica, *Ann. Geophys.*, 12, 1101–1113.

Crowley, G., B. A. Emery, R. G. Roble, H. C. Carlson, and D. J. Knipp (1989), Thermospheric dynamics during September 18–19, 1984: 2. Validation of the NCAR thermospheric general circulation model, *J. Geophys. Res.*, 94, 16,945–16,959, doi:10.1029/JA094iA12p16945.

Deng, Y., and A. J. Ridley (2006), Dependence of neutral winds on convection E-field, solar EUV, and auroral particle precipitation at high latitudes, *J. Geophys. Res.*, 111, A09306, doi:10.1029/2005JA011368.

Drob, D. P., et al. (2008), An empirical model of the Earth's horizontal wind fields: HWM07, *J. Geophys. Res.*, doi:10.1029/2008JA013668, in press.

Duboin, M.-L., and M. Lafeuille (1992), Thermospheric dynamics above Saint-Santin: Statistical study of the data set, *J. Geophys. Res.*, 97, 8661–8671, doi:10.1029/92JA00281.

Emery, B. A., C. Lathuillere, P. G. Richards, R. G. Roble, M. J. Buonsanto, D. J. Knipp, P. Wilkinson, D. P. Sipler, and R. Niciejewski (1999), Time dependent thermospheric neutral response to the 2–11 November 1993 storm period, *J. Atmos. Sol. Terr. Phys.*, 61, 329–350, doi:10.1016/S1364-6826(98)00137-0.

Emmert, J. T., B. G. Fejer, C. G. Fesen, G. G. Shepherd, and B. H. Solheim (2001), Climatology of middle- and low latitude F region disturbance neutral winds measured by Wind Imaging Interferometer (WINDII), *J. Geophys. Res.*, 106, 24,701–24,712, doi:10.1029/2000JA000372.

Emmert, J. T., B. G. Fejer, G. G. Shepherd, and B. H. Solheim (2002), Altitude dependence of mid and low latitude daytime thermospheric disturbance winds measured by WINDII, *J. Geophys. Res.*, 107(A12), 1483, doi:10.1029/2002JA009646.

Emmert, J. T., B. G. Fejer, G. G. Shepherd, and B. H. Solheim (2004), Average nighttime F region disturbance neutral winds measured by UARS WINDII: Initial results, *Geophys. Res. Lett.*, 31, L22807, doi:10.1029/2004GL021611.

Emmert, J. T., M. L. Faivre, G. Hernandez, M. J. Jarvis, J. W. Meriwether, R. J. Niciejewski, D. P. Sipler, and C. A. Tepley (2006a), Climatologies of nighttime upper thermospheric winds measured by ground-based Fabry-Perot interferometers during geomagnetically quiet conditions: 1. Local time, latitudinal, seasonal, and solar cycle dependence, *J. Geophys. Res.*, 111, A12302, doi:10.1029/2006JA011948.

Emmert, J. T., G. Hernandez, M. J. Jarvis, R. J. Niciejewski, D. P. Sipler, and S. Vennerstrom (2006b), Climatologies of nighttime upper thermospheric winds measured by ground-based Fabry-Perot interferometers during geomagnetically quiet conditions: 2. High-latitude circulation and interplanetary magnetic field dependence, *J. Geophys. Res.*, 111, A12303, doi:10.1029/2006JA011949.

Fejer, B. G., J. T. Emmert, G. G. Shepherd, and B. H. Solheim (2000), Average daytime F region disturbance neutral winds measured by UARS: Initial results, *Geophys. Res. Lett.*, 27, 1859–1862, doi:10.1029/2000GL003787.

Fejer, B. G., J. T. Emmert, and D. P. Sipler (2002), Climatology and storm-time dependence of nighttime thermospheric neutral winds over Millstone Hill, *J. Geophys. Res.*, 107(A5), 1052, doi:10.1029/2001JA000300.

Forbes, J. M., R. G. Roble, and F. A. Marcos (1987), Thermospheric dynamics during the March 22, 1979, magnetic storm: 2. Comparisons of model predictions with observations, *J. Geophys. Res.*, 92, 6069–6081, doi:10.1029/JA092iA06p06069.

Fuller-Rowell, T. J., M. V. Codrescu, R. G. Roble, and A. D. Richmond (1997), How does the thermosphere and ionosphere react to a geomagnetic storm?, in *Magnetic Storms*, Geophys. Monogr. Ser., vol. 98, edited by B. T. Tsurutani et al., pp. 203–225, AGU, Washington, D. C.

Fuller-Rowell, T. J., G. H. Millward, A. D. Richmond, and M. V. Codrescu (2002), Storm-time changes in the upper atmosphere at low latitudes, *J. Atmos. Sol. Terr. Phys.*, 64, 1383–1391, doi:10.1016/S1364-6826(02)00101-3.

Hedin, A. E. (1987), MSIS-86 thermospheric model, *J. Geophys. Res.*, 92, 4649–4662, doi:10.1029/JA092iA05p04649.

Hedin, A. E., N. W. Spencer, and T. L. Killeen (1988), Empirical global model of upper thermosphere winds based on Atmosphere and Dynamics Explorer satellite data, *J. Geophys. Res.*, 93, 9959–9978, doi:10.1029/JA093iA09p09959.

Hedin, A. E., et al. (1991), Revised global model of upper thermosphere winds using satellite and ground-based observations, *J. Geophys. Res.*, 96, 7657–7688, doi:10.1029/91JA00251.

Hedin, A. E., et al. (1996), Empirical wind model for the upper, middle, and lower atmosphere, *J. Atmos. Terr. Phys.*, 58, 1421–1447, doi:10.1016/0021-9169(95)00122-0.

Hernandez, G., and R. G. Roble (1976), Direct measurements of nighttime thermospheric winds and temperatures: 2. Geomagnetic storms, *J. Geophys. Res.*, 81, 5173–5181, doi:10.1029/JA081i028p05173.

Hernandez, G., F. G. McCormac, and R. W. Smith (1991), Austral thermospheric wind circulation and interplanetary magnetic field orientation, *J. Geophys. Res.*, 96, 5777–5783, doi:10.1029/90JA02458.

Holmes, S. A., and W. E. Featherstone (2002), A unified approach to the Clenshaw summation and the recursive computation of very high degree and order normalised associated Legendre functions, *J. Geod.*, 76, 279–299, doi:10.1007/s00190-002-0216-2.

Kawamura, S., Y. Otsuka, S.-R. Zhang, S. Fukao, and W. L. Oliver (2000), A climatology of middle and upper atmosphere radar observations of thermospheric winds, *J. Geophys. Res.*, 105, 12,777–12,788, doi:10.1029/2000JA900013.

Killeen, T. L., and R. G. Roble (1988), Thermospheric dynamics: Contributions from the first 5 years of the Dynamics Explorer program, *Rev. Geophys.*, 26, 329–367, doi:10.1029/RG026i002p00329.

Killeen, T. L., Y.-I. Won, R. J. Niciejewski, and A. G. Burns (1995), Upper thermosphere winds and temperatures in the geomagnetic polar cap: Solar cycle, geomagnetic activity, and interplanetary magnetic field dependences, *J. Geophys. Res.*, 100, 21,327–21,342, doi:10.1029/95JA01208.

McCormac, F. G., and R. W. Smith (1984), The influence of the interplanetary magnetic field Y component on ion and neutral motions in the polar thermosphere, *Geophys. Res. Lett.*, 11, 935–938, doi:10.1029/GL011i009p00935.

Meriwether, J. W. (2008), Thermospheric dynamics at low and mid-latitudes during magnetic storm activity, in *Midlatitude Ionospheric Dynamics and Disturbances*, Geophys. Monogr. Ser., vol. 181, edited by P. M. Kintner Jr. et al., AGU, Washington, D. C., in press.

Meriwether, J. W., J. P. Heppner, J. D. Stolarik, and E. M. Wescott (1973), Neutral winds above 200 km at high latitudes, *J. Geophys. Res.*, 78, 6643–6661, doi:10.1029/JA078i028p06643.

Morse, P. M., and H. Feshbach (1953), *Methods of Theoretical Physics*, McGraw-Hill, New York.

Niciejewski, R. J., T. L. R. Killeen, and S. C. Solomon (1996), Observations of thermospheric horizontal neutral winds at Watson Lake, Yukon Territory ($\Lambda = 65°$N), *J. Geophys. Res.*, 101, 241–259, doi:10.1029/95JA02683.

Rees, D. (1995), Observations and modelling of ionospheric and thermospheric disturbances during major geomagnetic storms: A review, *J. Atmos. Terr. Phys.*, 57, 1433–1457, doi:10.1016/0021-9169(94)00142-B.

Richmond, A. D. (1995), Ionospheric electrodynamics using magnetic apex coordinates, *J. Geomag. Geoelectr.*, 47, 191–212.

Richmond, A. D., and S. Matsushita (1975), Thermospheric response to a magnetic substorm, *J. Geophys. Res.*, 80, 2839–2850, doi:10.1029/JA080i019p02839.

Richmond, A. D., C. Lathuillere, and S. Vennerstroem (2003), Winds in the high-latitude lower thermosphere: Dependence on the interplanetary magnetic field, *J. Geophys. Res.*, 108(A2), 1066, doi:10.1029/2002JA009493.

Shepherd, G. G., et al. (1993), WINDII, the Wind Imaging Interferometer on the Upper Atmosphere Research Satellite, *J. Geophys. Res.*, 98, 10,725–10,750, doi:10.1029/93JD00227.

Sica, R. J., M. H. Rees, G. G. Romick, G. Hernandez, and R. G. Roble (1986), Auroral zone thermospheric dynamics: 1. Averages, *J. Geophys. Res.*, 91, 3231–3244, doi:10.1029/JA091iA03p03231.

Sica, R. J., G. Hernandez, B. A. Emery, R. G. Roble, R. W. Smith, and M. H. Rees (1989), The control of auroral zone dynamics and thermodynamics by the interplanetary magnetic field dawn-dusk (Y) component, *J. Geophys. Res.*, *94*, 11,921–11,932, doi:10.1029/JA094iA09p11921.

Spencer, N. W., L. E. Wharton, H. B. Hiemann, A. E. Hedin, G. R. Carignan, and J. C. Maurer (1981), The Dynamics Explorer wind and temperature spectometer, *Space Sci. Instrum.*, *5*, 417–428.

Sutton, E. K., J. M. Forbes, and R. S. Nerem (2005), Global thermospheric neutral density and wind response to the severe 2003 geomagnetic storms from CHAMP accelerometer data, *J. Geophys. Res.*, *110*, A09S40, doi:10.1029/2004JA010985.

Swarztrauber, P. N. (1993), The vector harmonic transform method for solving partial differential equations in spherical geometry, *Mon. Weather Rev.*, *121*, 3415–3437, doi:10.1175/1520-0493(1993)121<3415:TVHTMF> 2.0.CO;2.

Thayer, J. P., and T. L. Killeen (1993), A kinematic analysis of the high-latitude thermospheric neutral circulation pattern, *J. Geophys. Res.*, *98*, 11,549–11,565, doi:10.1029/93JA00629.

————————————

D. P. Drob and J. T. Emmert, Space Science Division, U.S. Naval Research Laboratory, Code 7643, 4555 Overlook Avenue SW, Washington, DC 20375, USA. (john.emmert@nrl.navy.mil)

G. Hernandez, Department of Earth and Space Sciences, University of Washington, Johnson Hall 070, Box 351310, 4000 15th Avenue NE, Seattle, WA 98195, USA.

M. J. Jarvis, British Antarctic Survey, High Cross, Madingley Road, Cambridge CB3 0ET, UK.

J. W. Meriwether, Department of Physics and Astronomy, Clemson University, 118 Kinard Laboratory, Clemson, SC 29634, USA.

R. J. Niciejewski, Space Physics Research Laboratory, University of Michigan, 2455 Hayward Street, Ann Arbor, MI 48109, USA.

G. G. Shepherd, Centre for Research in Earth and Space Science, York University, 4700 Keele Street, North York, ON M3J 1P3, Canada.

D. P. Sipler, Haystack Observatory, Massachusetts Institute of Technology, Off Route 40, Westford, MA 01886, USA.

C. A. Tepley, Arecibo Observatory, Cornell University, HC-03 Box 53995, Arecibo 00612, Puerto Rico.